ACTA IMEKO
ISSN: 2221-870X
June 2026, Volume 15, Number 2, 1 – 12

Flexible calibration method: Photometric and radiometric measurements with compact low-cost multi-channel sensors

Alberto Besozzi[1], Giovanni Gibertoni[1,2], Luigi Rovati[1], Agostino Gibaldi[1]

[1] *Department of Engineering "Enzo Ferrari", University of Modena and Reggio Emilia, 41125 Modena, Italy*
[2] *Department of Biomedical, Metabolic and Neural Sciences, University of Modena and Reggio Emilia, 41125 Modena, Italy.*

ABSTRACT
Compact multi-spectral sensors present a cost-effective solution for portable light measurement, yet their radiometric accuracy and spectral reconstruction capabilities remain under-characterised compared to laboratory-grade spectroradiometers. This study presents a systematic method for evaluating and calibrating a commercial sensor with a discrete set of spectral channels. The absolute radiometric responsivity was characterized using both laboratory-standard and readily accessible illumination sources, thereby demonstrating that the calibration is independent of the particular light source. Furthermore, the spectral power distribution reconstruction was evaluated under various illumination conditions, correctly estimating radiometric and photometric quantities for visual and non-visual systems. The results also show that increasing the number of spectral channels improves reconstruction accuracy primarily when the channels are well distributed over the spectral range, while additional overlapping bands provide only marginal benefits. This work is a step towards unified methodologies and infrastructure for standardised measurement tools and reproducible calibration.

Section: RESEARCH PAPER

Keywords: multi-spectral sensor; radiometric calibration; spectral power distribution; photometric measurements; α-opic

Citation: A. Besozzi, G. Gibertoni, L. Rovati, A. Gibaldi, Flexible calibration method: Photometric and radiometric measurements with compact low-cost multi-channel sensors, Acta IMEKO, vol. 15 (2026) no. 2, pp. 1–12. DOI: 10.21014/actaimeko.v15i2.2267

Section Editor: Maik Rosenberger, Ilmenau University of Technology, Germany

Received: December 12, 2025; **In Final Form:** April 30, 2026; **Published:** June, 2026.

Funding: This work has been partially supported by the grant Far Dipartimentale 2025 - FAR-DIP-GIBALDI from the University of Modena and Reggio Emilia, and by the Meta Reality Labs.

Corresponding Author: Alberto Besozzi, e-mail: alberto.besozzi@unimore.it

1. INTRODUCTION

In recent years, the demand for accurate measurements of both light intensity and spectral composition has expanded rapidly across a variety of scientific, biomedical, well-being and technological domains. To name a few examples, it has been used for wearable health sensors [1]–[3], distributed environmental monitoring [4]–[8], precision agriculture [9]–[14], portable diagnostic devices [15]–[18]. This expanding demand is closely related to the availability of emerging low-cost, miniaturised light-sensing technologies, which have enabled the integration of optical measurements into a broadening set of scientific and industrial applications.

In fact, traditional high-end devices (e.g., spectrophotometers, spectroradiometers) are designed to characterise light with exceptional precision, combining accurate reconstruction of the Spectral Power Distribution (SPD) and reliable radiometric intensity measurements. Despite the performance, these devices tend to be bulky and expensive, require careful calibration, controlled conditions, and depend on wall power. These characteristics make them rarely suited for continuous, distributed, or wearable measurement, where miniaturisation, low cost, portability, and robustness are required.

Compact multi-spectral sensors have gained increasing attention as low-cost alternatives to traditional spectrometers [7], [19], [20]. These devices integrate interference filters directly on silicon, providing a small number of fixed spectral bands, varying from 3 channels (S9032 from Hamamatsu) to 18 channels (AS7265x from OSRAM). These sensors can also vary in dimension, usually a couple of millimeters for the sensor alone, and price, from a few dollars to hundreds. Although inexpensive and highly portable, they exhibit complex spectral responses and non-uniform sensitivities across illumination levels. Moreover, their performance depends strongly on their configuration and usage, namely integration time and digital gain. These factors create the need for accurate calibrations to enable their practical use, like accurate SPD reconstruction and the measurement of radiant power or illumination [6]–[8], [20]–[23].

To contextualize, this need for robust calibration is under-

scored by recent expert consensus highlighting critical gaps in the field of light metrology [2], [3], [20]–[22], [24], [25]. As detailed by Spitschan and colleagues, the current landscape of ocular light and optical radiation exposure research is fragmented, lacking standardised measurement tools and reproducible calibration protocols. Furthermore, the consensus identifies significant deficiencies in the collection of contextual information. For instance, direct measurement of gaze direction has been shown to yield rich information about the visual content reaching the retinas, including fixation distance [26], retinal blur [27], and the spatio-temporal characteristics of the viewed environment [28]. Accordingly, comparable benefits are anticipated for understanding the spatial distribution of light. Another critical point in this research field is the lack of standardised outcome measures and data-logging strategies [24]. This lack of unified methodologies and infrastructure complicates data harmonisation and obstructs the comparability of results across studies.

In this context, a calibration method that allows to use a single multi-channel sensor to contextually obtain different measures, from an accurate reconstruction of the SPD, to reliable radiometric intensity measurements, is proposed. Unlike conventional methods that rely on monochromators, tunable sources, or highly stable laboratory lamps [29], the proposed approach takes advantage of a generalising calibration procedure that can be obtained using readily available natural or commercial light sources. This not only reduces the barrier to adoption but also supports field calibration and re-calibration, an increasingly important requirement for mobile, wearable, and distributed sensing platforms.

In detail, this study will focus on the following elements:

- the development of a mathematically grounded calibration method compatible with compact sensors characterised by broad or overlapping spectral responsivities [30]–[32],
- An evaluation of the accuracy and stability of the method across different sensor configurations, but also light sources, intensities, and environmental conditions,
- the demonstration of applicability in real cases of both spectral reconstruction and quantitative irradiance estimation, enabling the computation of radiometric, photometric, and biologically relevant light metrics,
- demonstration of the robustness and adaptability of the calibration procedure by performing it with a readily available natural or commercial light source,
- considerations for practical deployment, including sensor constraints, noise sources, and the feasibility of natural-light calibration workflows.

In summary, the proposed methodology aims to clarify the achievable accuracy and limitations of low-cost multi-spectral sensors, as well as to provide practical guidelines for their integration into sensing and measurement systems.

2. RELATED WORKS

Several approaches have been proposed in the literature to reconstruct the Spectral Power Distribution (SPD) using compact multi-spectral sensors.

Some works have focused on high-performance compact or miniature spectrometers, which offer higher spectral resolution at substantially higher cost, like C12666MA and C10988MA-1 (Hamamatsu Photonics K.K., Hamamatsu City, Japan). Mohamed et al. [21] used a device based on the C12666MA to develop a spectral sensor for measuring daily light exposure. Their system was calibrated it with a Konica Minolta CL-500A (Konica Minolta, Inc., Tokyo, Japan) spectroradiometer while compensating for nonlinearities in integration time and stray light. Gibertoni et al. [23] used the C10988MA-1 for the radiometric calibration in ophthalmic systems, for delivering a controlled multi-wavelength stimulation. Although these miniature spectrometers provide excellent accuracy, their cost, typically several hundred euros, limits their suitability for low-cost sensing or embedded applications.

Stampfli et al. [22] applied a similar approach to the HOBO UA-002-64 (Onset, Bourne MA, USA) device, using a Specbos spectroradiometer as a reference instrument. Their calibration method achieved a relative error below 5 % in illuminance measurements, demonstrating the feasibility of cost-effective light-intensity sensing through regression-based compensation.

Amirazar et al. [20] employed an AS7265X (ams-OSRAM AG, Premstaetten, Austria) sensor calibrated using multiple reference light sources (LEDs, daylight, incandescent and fluorescent lamps) together with a WaveGO spectrometer and an integrating sphere. Weighting factors for each visible channel were optimised to fit the reference SPD, and then used an artificial neural network to reconstruct the spectrum over a [380,780] nm range, achieving an error below 17 %.

Gibaldi et al. [29] developed a head-mounted system to collect statistics of visual experience in children, for evaluating environmental risk factors for myopia. For light sensing they used the AS7262, and they calibrated it using a monochomator creating narrow-band light in 10 nm steps from 380 to 780 nm, verified against a Photo Research PR-650 SpectraScan Colorimeter.

Mohammadian et al. [25] calibrated an AS7341 sensor using combined violet and white LED sources filtered through selectable band-pass filters, with a SpectroCAL MKII spectrometer (Cambridge Research Systems Ltd., Rochester, UK) serving as reference, reporting overall errors below 15 %.

Myland et al. [7] used the AS7341 sensor for real-time monitoring of indoor lighting to allow for a dynamic tuning of light quality to maintain optimal or intended conditions. Specifically, they trained a convolutional neural network to obtain a reconstruction of the SPD. The dataset was obtained collecting real-world indoor data with the AS7341 against a small spectro-radiometer (CSS45, Gigahertz Optik GmbH, 82299 Tuerkenfeld, Ge), used as ground truth. Despite the high accuracy in reconstructing the SPD (average of 2.7 %), this approach is implicitly prone to classification errors, thus misrepresenting the actual spectrum.

Kristiansen et al. [8] used AS7265x multi-spectral sensor, endowed with 21 channels, to monitor the spectral composition of light in indoor environments. Their calibration was performed using wide and narrow band light sources against a GL Spectis 1.0 Touch spectroradiometer, achieving an average spectral accuracy of 9.3 %. The rigorous and effective method comes to the price of the requirement of a controlled and high-end setup, *e.g.* the Abet Technologies Sun 2000 to simulate natural light from the sun.

Overall, existing studies demonstrate the potential of both multi-spectral sensors and compact spectrometers for SPD estimation. However, several limitations remain. First, calibration procedures are often specific to a single device or illumination condition, limiting reproducibility. Second, comparisons across sensors with different numbers of channels are scarce. Third, few works evaluate performance under both controlled laboratory conditions and realistic outdoor or indoor illumination.

3. MATERIALS AND METHODS

Multi-channel spectrometers excel at capturing relative spectral variations; however, they inherently lack the capability for direct absolute intensity measurement. To enable accurate radiometric quantification, a rigorous calibration procedure is essential.

In this work, two specific experiments to characterise the behavior of these devices are presented: Experiment 1 (Section 3.4.) investigates channel stability as a function of internal analog gain and integration time, aiming to identify the optimal strategy for dynamic range adjustment; Experiment 2 (Section 3.5.) focuses on quantifying absolute radiometric sensitivity across varying irradiance levels.

3.1. Multi-spectral sensors under test

Three compact multi-spectral sensors from ams OSRAM were evaluated in this study: the AS7262, the AS7341, and the AS7343. All devices integrate nano–optic interference filters directly on CMOS silicon, have six built-in 16 bit ADC and provide digital output via an I^2C interface, enabling low-power and small-footprint spectral measurements suitable for wearable, compact and portable instrumentation.

The AS7262 is a 6-channel visible spectral sensor providing narrowband responses at approximately 450, 500, 550, 570, 600, and 650 nm [30].

The AS7341 is an 11-channel sensor covering roughly [350,1000] nm [31]. It includes eight visible channels, one NIR channel, one clear channel, and a dedicated flicker channel for ambient-light modulation detection. Only the visible and clear channels were used in this work.

The AS7343 is a 14-channel device featuring eleven visible bands, one NIR channel, one visible channel and one flicker channel [32]. Compared with the AS7341, it offers denser sampling of the visible range and improved sensitivity, enabling more accurate spectral reconstruction and more robust operation under low-light conditions.

All sensors were tested using commercially available breakout boards (AS7262 and AS7341 from Adafruit; AS7343 from Pimoroni), which provide stable mechanical mounting, integrated voltage regulation and level shifting. The boards were interfaced to an ESP32-S3 microcontroller board via I^2C. Raw channel counts, gain values and integration times were streamed to a host computer for offline calibration and analysis.

Even if this analysis has been carried on for the three specified sensors, the calibration process has been devised to be general reproducible on other multi-channel spectrometers.

3.2. Optical sources, filtering and reference instruments

A diverse set of broadband optical sources was employed throughout the experiments to cover a wide range of spectral profiles. All selected emitters provide wide spectral coverage in the visible range.

The primary calibrated broadband source was the SLS401 xenon short-arc lamp (Thorlabs Inc., Newton, NJ, USA), specified for the [240,2400] nm range with a colour temperature of 5800 K and typical output power above 1.3 W. The lamp offers power stability better than 0.3 % over one hour and a typical drift of 0.1 % per hour after warm-up, and includes an internal collimation stage producing a 35 mm diameter free-space beam.

Two tungsten–halogen lamps from the HL-2000 series (Ocean Optics, Largo, FL, USA) [33] were used to provide additional broadband visible spectra:

- HL-2000-FHSA, a long-lifetime 7 W halogen lamp (typical output 4.5 mW, 2800 K).
- HL-2000-HP, a high-power 20 W halogen lamp (typical output 8.8 mW, 3000 K).

Both lamps cover the [360,2400] nm range and exhibit output stability better than 0.25 % peak-to-peak and drift below 0.1 % per hour after warm-up.

A white high-power LED (XLamp MX-6, model MX6AWT-A1-0000-0009E8; Cree LED, Durham, NC, USA) [34] was also employed as an additional broadband illuminant. In particular, it includes multiple internal emitters (blue, green and red), resulting in a combined broadband output.

The HL-2000-FHSA, HL-2000-HP and MX-6 LED sources were coupled to a collimating optics stage (achromatic lens and adjustable aperture) to obtain a quasi-uniform beam at the sensor plane. In all cases, the beam diameter at the sensor plane was set larger than the active aperture of the sensors to minimise alignment sensitivity.

All optical sources were filtered using an FGS900H KG3 colored-glass bandpass filter ([315,710] nm; Thorlabs Inc., Newton, NJ, USA) [35]. This filter was employed to restrict the incident beam to the visible range and suppress near-infrared components, ensuring consistent spectral integration between the broadband reference instruments and the visible-light sensors. It is worth noting that for standalone applications of the multi-spectral sensors, this additional filtration is not strictly necessary, as the individual channels are designed to be insensitive to wavelengths outside their target bands. For the SLS401 source, additional irradiance levels were produced using step variable neutral-density filter (model NDC-50S-1 - Step Variable ND Filter, Ø50 mm, OD: 0.04-1.0 ; Thorlabs Inc., Newton, NJ, USA) [36].

Two calibrated instruments provided spectral and radiometric reference measurements:

- Qmini AFBR-S20M2WU spectrometer (Broadcom Inc., San José, CA, USA), covering [225,1000] nm [37].
- PM16-130 optical power meter (Thorlabs Inc., Newton, NJ, USA) [38], used to measure the total irradiant optical power.

Spectrometer and power-meter readings were combined to obtain the absolute spectral irradiance at the sensor plane for each calibration condition.

Table 1 summarises the full set of optical configurations employed in the calibration campaign.

Table 1. Overview of optical configurations used in the two experiments.

Config	Source	Optical filtering	Notes
C1	SLS401 (xenon)	FGS900H	Reference irradiance
C2	SLS401 (xenon)	FGS900H + ND 0.04	Reduced level 1
C3	SLS401 (xenon)	FGS900H + ND 0.1	Reduced level 2
C4	SLS401 (xenon)	FGS900H + ND 0.2	Reduced level 3
C5	SLS401 (xenon)	FGS900H + ND 0.3	Reduced level 4
C6	SLS401 (xenon)	FGS900H + ND 0.4	Reduced level 5
C7	SLS401 (xenon)	FGS900H + ND 0.5	Reduced level 6
C8	SLS401 (xenon)	FGS900H + ND 0.6	Reduced level 8
C9	HL-2000-FHSA	FGS900H	Broadband halogen, lower output
C10	HL-2000-HP	FGS900H	Broadband halogen, higher output
C11	MX-6 LED	FGS900H	Broadband LED

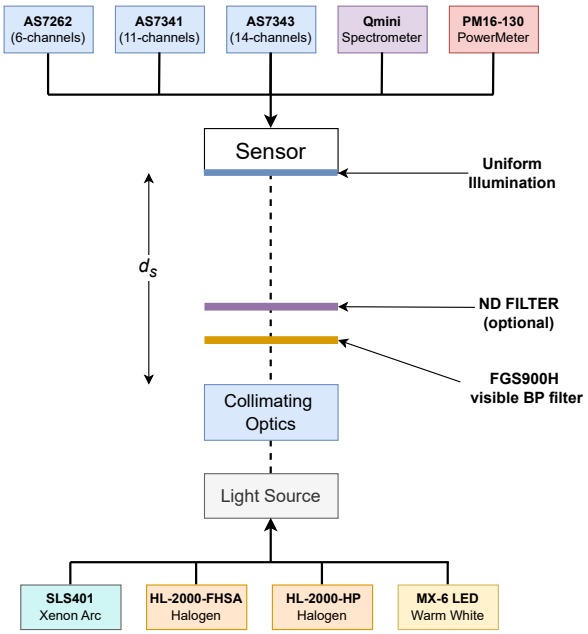

Figure 1. Optical setup used for experiments 1 and 2. A xenon, halogen or LED source illuminates the detector plane from a distance $d_s = 60\,\mathrm{mm}$, through ND filters (optional) and the FGS900H visible filter. Halogen and LED sources are collimated externally, whereas the SLS401 provides a factory-collimated output. For each configuration (C1–C11 in Table 1), a single sensing element (AS7262, AS7341, AS7343, Qmini, or PM16-130) was placed at the same physical location on the optical table, replacing the previous detector while source and optics remained fixed.

3.3. Mechanical arrangement and common optical setup

All measurements were performed on a rigid metric optical table that ensured reproducible alignment of the light source, filters, collimation optics and detector plane. The distance between the output of the source and the measurement plane, denoted as d_s in Figure 1, was fixed to 600 mm for all calibration configurations.

Each sensing element—the three multispectral sensors, the spectrometer fiber, and the power-meter detector—was placed individually in the same measurement position. For every optical configuration (C1 to C11; see Table 1), one detector at a time was mounted in that fixed location on the optical bench, replacing the previous one while the source, filters, and collimating optics remained unchanged. This procedure ensured that all devices sampled the same portion of the beam, under identical geometric and radiometric conditions.

The AS7262, AS7341, AS7343, the Qmini spectrometer and the PM16-130 detector head were all referenced to the same measurement plane, with the entrance apertures positioned within a few millimetres of one another. Each device was oriented orthogonally to the incoming beam to minimise angular-dependence artefacts.

A schematic of the optical setup used for experiments 1 and 2 is shown in Fig. 1. The diagram illustrates the fixed positions of the source, filters and optics, and the interchangeable position where each sensing element was sequentially mounted.

3.4. Experiment 1: channel stability vs gain and integration time

Since the firmware of each sensor allows for different possible configurations in terms of gain (G) and integration time (t_{int}), the first experiment evaluated the stability of each spectral channel when varying sensor configuration under fixed illumination. Refers to Table 2 for combination of G and t_{int} used for each sensor and each optical configuration (C1–C11 in Table 1). For every combination of source, G and t_{int}, twenty repeated measurements were recorded for each channel to reduce noise.

Only samples producing a raw count between 10% and 80% of the full-scale (FS) range were retained to ensure operation within the linear region of the ADC, so some pairs reported in Table 2 have been removed from the analysis. Only measurements yielding raw counts between 10 % and 80 % of the full-scale (FS) range were retained. Values below approximately 10 % FS are dominated by quantisation noise, dark-count variability, and instabilities in the internal analog chain, whereas values above 80 % FS may exhibit compressive non-linearity and soft saturation of the ADC. Restricting the analysis to this interval ensures that all channels operate within their most linear and repeatable region, in line with previous work showing that both low-end and near-saturated readings introduce substantial non-linearity and uncertainty [6], [24]. For this reason, some gain/integration-time combinations listed in Table 2 were excluded from the analysis when their corresponding measurements fell outside this valid operating range.

Table 2. Gain and integration-time settings used in Experiment 1 to check for variability in the measurement. Integration times are expressed in milliseconds.

Sensor	Gain values	Integration times (ms)
AS7262	1, 3.7, 16, 64	5, 10, 15, 20, 30, 40, 50, 75, 100, 150, 200
AS7341	0.5, 1, 2, 4, 8, 16, 32, 64, 128, 256, 512	5, 10, 15, 20, 30, 40, 50, 75, 100, 150, 200
AS7343	0.5, 1, 2, 4, 8, 16, 32, 64, 128, 256, 512, 1024, 2048	5, 10, 15, 20, 30, 40, 50, 75, 100, 150, 200

To compare the responses obtained under different acquisition parameters, each raw count c was first normalised by the corresponding gain and integration time

$$\tilde{c} = \frac{c}{G\, t_{\mathrm{int}}}. \tag{1}$$

since under ideal operating conditions, and with the source held constant, altering the internal configuration of the sensor should produce a linear change in its response.

Within each optical configuration (C1–C11), channels naturally exhibit different absolute responses due to their spectral sensitivities and the shape of the illumination spectrum. To remove these differences, the normalised measurements from each channel were further normalised by the mean value of that channel within the same configuration. This produced dimensionless values centered around 1 for each channel in every configuration, allowing direct comparison across all gain and integration times and across all illuminations.

After this two-stage normalisation, the measurements from all configurations were first compared separately by gain and by integration time, yielding two distinct sets of data: the first captures the sensor behavior with fixed gain while varying the integration time, and the second does the reverse. In this way, measurements from different configurations become comparable; To isolate random noise and exclude transient artefacts, a Z-score outlier detection method was applied to the raw counts. Measurements exhibiting a Z-score greater than 1 were excluded from the analysis to ensure a strict quality threshold for calibration data. Then, for each configuration, sensor and channel, the Coefficient of Variation (CV) has been extracted over the entire range of gains G (Eq. 2, N is

the number of measures at each gain, which corresponds to the eleven possible integration times) and integration times t_{int} (Eq. 3, M is the number of measures at each t_{int}, which corresponds to the number of possible gain, four for the AS7262 sensor, eleven for the AS7341 and AS7343). This coefficient is defined as the Standard Deviation ($\sigma_{\tilde{c}}$) divided over the mean reading ($\mu_{\tilde{c}}$), for each channel.

$$CV(t_{\mathrm{int}})\big|_{\mathrm{ch}=x} = \frac{\sigma_{\tilde{c}}}{\mu_{\tilde{c}}} = \frac{\sqrt{\frac{1}{N-1}\sum_{i=1}^{N}(\tilde{c}_i - \mu_{\tilde{c}})^2}}{\frac{1}{N}\sum_{i=1}^{N}\tilde{c}_i} \tag{2}$$

$$CV(G)\big|_{\mathrm{ch}=x} = \frac{\sigma_{\tilde{c}}}{\mu_{\tilde{c}}} = \frac{\sqrt{\frac{1}{M-1}\sum_{i=1}^{M}(\tilde{c}_i - \mu_{\tilde{c}})^2}}{\frac{1}{M}\sum_{i=1}^{M}\tilde{c}_i} \tag{3}$$

$$\begin{aligned} \tilde{CV}(t_{\mathrm{int}}) &= \frac{1}{C}\sum_{x=1}^{C} CV(t_{\mathrm{int}})\big|_{\mathrm{ch}=x} \\ \tilde{CV}(G) \quad &= \frac{1}{C}\sum_{x=1}^{C} CV(G))\big|_{\mathrm{ch}=x} \end{aligned} \tag{4}$$

where $\tilde{CV}$ represent the Coefficient of Variation averaged over the number of channels C.

3.5. Experiment 2: Calibration of absolute radiometric sensitivity in Lab setup

The second experiment estimated the absolute radiometric sensitivity of each channel using the SLS401 source at eight different irradiance levels (C1–C8, denoted as Dataset 1). In this case, Xenon arc lamp provided the most uniform broadband illumination across the whole visible range, thus improving measure accuracy. It is worth noting that alternative broadband sources can also be employed in this procedure, as long as they emit substantial light across all spectral bands of interest. For each level of illumination, the spectral irradiance $E(\lambda)$ at the sensor plane was obtained as follows:

1) The Qmini spectrometer measured the dimensionless spectral distribution of the beam at the position of the sensor plane.
2) The PM16-130 power meter measured the current generated by the incident light, which is then converted to irradiance ($\mathrm{W/m^2}$) using its internal responsivity and the area of the sensing element.
3) The spectral distribution was scaled so that its integral over wavelength equaled the reading of the power-meter divided by the collection area, producing spectral irradiance ($\mathrm{W/(m^2 \cdot nm)}$).

For each sensor, the datasheets [30]–[32] specify the spectral sensitivity of every channel i, modeled as a Gaussian profile characterized by a central wavelength λ and a Full Width at Half Maximum (FWHM). The datasheets also include an example of the typical response to a given spectrum, but this is a qualitative functioning example and cannot be taken as a reliable reference for the absolute responsivity of the channels. Therefore, to determine the effective optical power incident on each channel, this process relied solely on the nominal spectral responsivity curve $S_i(\lambda)$ provided in the respective datasheet:

$$P_i = \int_{\lambda_{\min}}^{\lambda_{\max}} E(\lambda)\, S_i(\lambda)\, \mathrm{d}\lambda \tag{5}$$

expressed in $\mathrm{W/m^2}$, where the integration limits were restricted to the visible range (typically [380,780] nm).

For each irradiance level and channel, the gain/IT-scaled counts $\tilde{c}_i$ were computed as in Eq. 1. A quadratic model

$$\tilde{c}_i = a_i\, P_i^2 + b_i\, P_i + d_i \tag{6}$$

was then fitted by least squares over the four irradiance levels, where the coefficients a_i and b_i represents the sensitivity of channel i based on the irradiance level P_i, and d_i accounts for residual offsets and dark counts. The fitted coefficients were used to scale the nominal spectral responsivity curves and to reconstruct the spectral irradiance for each channel. The quadratic fit was chosen over the linear fit because it yields a substantially higher coefficient of determination (R^2).

3.5.1. Spectral reconstruction model

Following channel-wise sensitivity correction, the discrete set of n measures, being n the number of spectral channel, must be used to reconstruct the SPD of the incident light. A straightforward approach involves summing the Gaussian response profiles of all channels. However, due to overlap between adjacent channels, this method is likely to result in an overestimation of spectral power and yield inaccurate measurements, especially in high density channels (like the AS7343). A more refined strategy entails avoiding double-counting in regions of overlap, by considering only the most sensitive channel for each wavelength of the considered spectrum. While this approach mitigates overestimation, it can introduce gaps in the reconstructed spectrum, particularly for spectrometers with lower channel density (such as the AS7262) where spectral intervals between channels may remain unrepresented. One possible solution to mitigate this gaps, for applications involving broadband light sources, is the implementation of a regularisation procedure, which enhances the continuity and fidelity of the reconstructed spectral profile, to match the original one. In particular the regularisation can be obtained solving the following equation:

$$W = \left[(X^{\mathrm{T}}X + t\, I)^{+} X^{\mathrm{T}} y\right]^{\mathrm{T}} \tag{7}$$

which provide a set of weights (W) to be applied to the channel measurement, starting from the gaussian functions of each channel (X) and the target SPD (y). t is a coefficient used for the regularisation, here fixed to $1 \cdot 10^{-8}$.

Alternatively, a distinct approach for profile reconstruction involves applying Piecewise Cubic Hermite Interpolating Polynomial (PCHIP) interpolation directly to the peaks of the Gaussian profiles. Unlike previous methods, this technique explicitly disregards the specific geometry of the Gaussian shape, operating on the premise that the responsivity calibration performed in Experiment 2 has already sufficiently accounted for sensitivity variations. In high density channels spectrometers, an additional smoothing can be performed to avoid jumps between close channels with high differences.

In the following section, the performance of these reconstruction methodologies is systematically evaluated and compared.

3.6. Validation of Experiment 2: Figure of merits extraction in Real-world measurements

To evaluate performance under realistic illumination, the calibrated reconstruction model was tested in three distinct real-world scenarios:

- outdoor sunlight illumination;
- indoor LED illumination in laboratory and domestic environments;

- emission from a white display source (monitor or panel).

For each scenario, the three multi-spectral sensors, the spectrometer and the power meter were mounted on the same mechanical structure, with the FGS900H filter placed in front of the assembly. Each sensor was operated using the gain identified during calibration as providing the most accurate and stable response for broadband visible light.

To quantify the reconstruction accuracy, two primary figures of merit were extracted. First, the overall fidelity of the spectral shape was assessed using the Root Mean Square Error (RMSE) between the reconstructed and reference SPDs. Second, a normalized spectral distribution error was computed for key radiometric, photometric, and colorimetric quantities, specifically: total irradiance, illuminance, and the five α-opic irradiances (S-, M-, L-cone, rhodopic, and melanopic). This metric was derived by calculating the absolute error at each wavelength before aggregation, rather than simply comparing the final integrated values. The mean of these absolute spectral differences was then normalized by the mean value of the reference quantity. This formulation prevents the mutual compensation of under- and over-estimation errors that typically occurs in standard integral comparisons, thereby providing a stricter and more distributed measure of spectral accuracy.

3.7. Experiment 3: Calibration of absolute radiometric sensitivity with different sources

As noted in Section 3.5., the radiometric calibration is theoretically independent of the specific broadband source employed, provided the source covers the relevant spectral bands. To validate this assumption and evaluate the broader applicability of the quadratic model (Eq. 6), the experimental dataset was extended to include conditions beyond the Xenon arc lamp configurations.

Three illumination sources (two Halogen and one white LED, C9–C11), characterized by distinct spectral power distributions, were introduced to the fitting process together with three configurations from the previous Xenon setup (C1–C3). The quadratic regression was re-evaluated using this dataset (denoted as Dataset 2), and the variations in the quadratic fitting coefficients (a_i, b_i, and d_i) and the figures of merit (described in Section 3.6.) from the calibration performed by Dataset 1 and Dataset 2, has been compared. Minimal deviation in these metrics would indicate that the sensor's response is determined mainly by the effective integrated optical power (P_i), rather than the specific spectral profile of the incident light, thus validating the robustness and versatility of the calibration procedure.

4. RESULTS AND DISCUSSION

4.1. Experiment 1: Channel stability and acquisition parameters

The stability of the multi-spectral sensors was evaluated by analysing the variation in normalised response across different G and t_{int} settings. As detailed in Section 3., the objective was to identify the optimal strategy for dynamic range adjustment—specifically, whether to modulate sensitivity via gain or integration time.

Table 3 presents the Coefficient of Variation when the gain was held constant while sweeping the integration time (all the gains presented in Section 3.4. has been used). The results indicate a high degree of linearity and stability. Across all optical configurations (ordered by progressively lower irradiance levels), the CV for all three sensors remained in the order of 10^{-4}. This suggests that the sensors' response scales linearly with integration time, introducing negligible non-linearity errors when t_{int} is used to adjust the sensitivity.

Conversely, Table 4 summarises the performance when the integration time was held constan while sweeping the gain values (all the t_{int} presented in Section 3.4. has been used). In this scenario, the CV were significantly higher, typically in the range of 10^{-3} to 10^{-2}. In particular, the AS7343 and AS7262 exhibited a standard deviation approximately two orders of magnitude higher than that observed in the constant-gain experiments.

Table 3. Coefficient of Variation at constant gain and variable integration time, $\tilde{CV}(t_{\mathrm{int}})$ Eq. 4. The first number is the average over the number of channels, the range on the side represent the minimum and maximum value across the channels

Config	Irradiance ($\mu W/cm^2$)	$\tilde{CV}(t_{\mathrm{int}}) \cdot 10^{-4}$		
		AS7262	AS7341	AS7343
C1	761.77	0.80 (0.38–2.44)	1.17 (0.40–2.32)	4.32 (3.32–6.92)
C2	651.18	0.84 (0.42–2.35)	1.08 (0.55–1.68)	3.22 (2.30–5.36)
C3	547.23	1.20 (0.87–1.96)	1.16 (0.72–1.57)	3.74 (2.77–5.53)
C4	466.34	1.08 (0.74–1.87)	1.22 (0.79–1.97)	3.51 (2.59–5.28)
C5	391.08	1.73 (1.18–3.03)	1.73 (1.24–2.53)	3.52 (2.48–5.20)
C6	342.17	1.56 (1.04–2.77)	1.67 (1.16–2.36)	3.41 (2.41–5.19)
C7	272.74	1.42 (0.92–2.62)	1.62 (1.12–2.26)	3.35 (2.29–4.92)
C8	186.95	1.44 (0.83–3.33)	1.55 (1.05–2.16)	3.20 (2.19–4.66)

Table 4. Coefficient of Variation at constant integration time and variable gain, $\tilde{CV}(G)$ Eq. 4. The first number is the average over the number of channels, the range on the side represent the minimum and maximum value across the channels

Config	Irradiance ($\mu W/cm^2$)	$\tilde{CV}(G) \cdot 10^{-4}$		
		AS7262	AS7341	AS7343
C1	761.77	270.42 (260.15–298.50)	23.72 (19.14–26.88)	340.98 (195.76–641.76)
C2	651.18	273.15 (254.20–307.12)	23.49 (18.55–26.24)	337.15 (198.15–624.89)
C3	547.23	275.58 (258.55–303.85)	23.82 (18.66–26.54)	360.33 (209.57–682.63)
C4	466.34	268.21 (257.40–288.66)	23.24 (17.47–25.53)	388.76 (222.73–756.67)
C5	391.08	272.85 (256.55–301.34)	23.30 (16.93–25.79)	408.90 (228.14–825.43)
C6	342.17	264.26 (247.89–292.30)	27.08 (20.51–29.67)	414.90 (227.74–857.72)
C7	272.74	261.10 (244.85–288.41)	30.17 (22.77–32.65)	392.48 (215.06–815.05)
C8	186.95	258.32 (241.83–285.51)	31.86 (24.85–34.58)	375.05 (205.61–778.69)

Comparing the two acquisition strategies, it is evident that keeping the gain constant yields superior stability and lower variance. Varying the gain amplifies signal variations and introduces non-linearities that complicate the estimation of absolute responsivity. Consequently, to maximise the dynamic range while maintaining radiometric accuracy, the optimal strategy for these sensors is to fix the internal analog gain and modulate the exposure solely via the integration time. Based on these findings, the subsequent determination of absolute responsivity (Experiment 2) was performed using a fixed gain configuration (64X) for each sensor, relying on integration time adjustments to accommodate varying irradiance levels.

4.2. Experiment 2: Absolute radiometric sensitivity and spectral reconstruction

Following the characterization of acquisition parameters, the absolute radiometric sensitivity was extracted for each channel. As described in Section 3.5., the effective optical power incident on each channel was weighted by the channel's specific sensitivity curve (here extracted from the reference datasheet [30]–[32]) to ensure the measurement values corresponded to the actual optical power absorbed by the filtered channels (Eq. 5)

Initially, a linear fitting model was evaluated to characterize the relationship between incident optical power and sensor output. However, this approach yielded suboptimal goodness-of-fit metrics compared to the quadratic model. While the AS7341 sensor maintained moderate linearity ($R^2 \approx 0.98$), the AS7262 and AS7343 exhibited more pronounced non-linear behavior. The AS7343, in particular, showed the poorest linear correlation, with R^2 values dropping as low as 0.86 in the worst-performing channels. Overall, the linear fit resulted in coefficients of determination ranging from 0.86 to 0.99 across all sensors, with poorer values compared to the quadratic fitting (detailed tabular results are provided in the Appendix). These deviations necessitated the

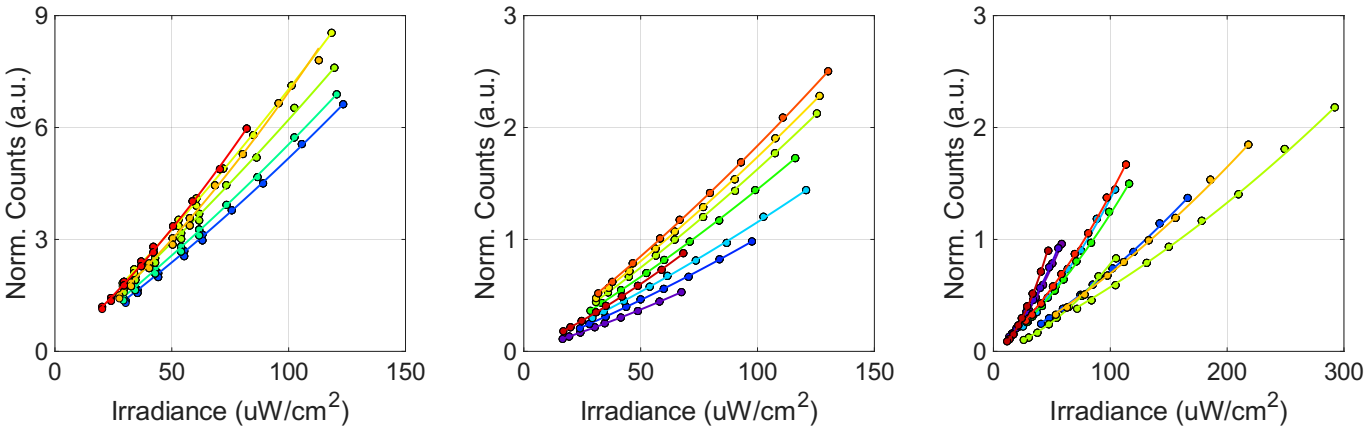

Figure 2. Quadratic calibration curves representing the responsivity of the AS7262 (a), AS7341 (b), and AS7343 (c) spectrometers. Note that, for visualization purposes, the x- and y-axes do not share the same range across the three plots.

adoption of a higher-order polynomial to accurately model the acquisition chain.

The response of each channel was then modeled using the quadratic function defined in Eq. 6, using Dataset 1 as the reference. Since the sensors exhibited negligible output in the absence of illumination, the offset coefficient d_i was forced to 0, reducing the model to a two-parameter fit (a_i, b_i).

Figure 2 illustrates the relationship between the measured raw counts (y-axis) and the effective irradiance reaching each channel (x-axis). The tightness of the data points along the fitted curves confirms the validity of the quadratic model. This is quantitatively supported by the R^2 values for all channels across the three sensors, which are summarised in Table 5. The R^2 values are consistently above 0.998, indicating an excellent fit between the model and the experimental data.

Table 5. Goodness-of-fit (R^2) values for the quadratic radiometric calibration of each channel. GAIN = 64x

Channel	AS7262	AS7341	AS7343
1	0.99982	0.99981	0.99902
2	0.99985	0.99980	0.99919
3	0.99977	0.99964	0.99916
4	0.99992	0.99989	0.99847
5	0.99939	0.99997	0.99875
6	0.99917	0.99985	0.99872
7	–	0.99982	0.99908
8	–	0.99987	0.99896
9	–	–	0.99912
10	–	–	0.99828

4.2.1. Qualitative evaluation of spectral reconstruction methods

Using the calibrated sensitivity parameters, the spectral power distribution of various light sources was reconstructed using the three methodologies outlined in the methods: Gaussian profile envelope (ENV), Regularisation profile (REG), and Smoothed pchip profile (SMT).

Figure 3 displays the reconstruction performance for the AS7343 sensor under four distinct illumination conditions: halogen, LED, sunlight, and xenon lamp. The other two sensor profiles are not reported for simplicity, while the numerical comparison for all three sensors is reported in Table 6. The ENV profile accurately captures the spectral power at the centre wavelengths of the channels; however, it fails to represent the continuum between channels, resulting in significant underestimation in the spectral gaps. This artifact is particularly pronounced in the AS7262 due to its lower channel density, whereas the AS7343 offers a denser sampling that mitigates this effect.

The REG profile provides a continuous spectrum that matches the reference well. However, its performance is inherently dependent on the training set used to derive the weights; it excels when the test source resembles the calibration sources but may deviate for unknown spectral signatures.

The SMT profile, based on pchip interpolation, yielded a good representation of the reference curves. It generates a continuous spectrum without requiring previous knowledge of the source type (source-independent). As illustrated in Fig. 3, it successfully fills the gaps between channel peaks while preserving radiometric accuracy, with the exception of the LED spectrum, where the pronounced peak near 450 nm is not accurately reconstructed. This occurs because the total power of that peak is spread out according to the Gaussian profile of the spectrometer's nearest channel.

4.3. Quantitative evaluation and figures of merit

Before evaluating the global performance of the sensors for each reconstruction method, the spectral distribution of the reconstruction error was analysed. To visualise the error dependence on wavelength, the relative spectral error was computed and aggregated into ten distinct bins of 40 nm width. Figure 4 illustrates the mean relative percent error within each spectral bin. It is evident that the error increases drastically for all sensors in the regions falling outside their primary sensitivity range, specifically in the [380,420] nm and [700,780] nm intervals.

Consequently, to ensure a valid assessment, the subsequent analysis was restricted to the effective spectral range where the sensors are active. Within this valid range, the accuracy of the reconstruction methods is summarised in Table 6, which presents the mean RMSE of the spectral content and the mean relative error for key radiometric and photometric quantities, including total spectral irradiance, illuminance, and the effective irradiances for the five retinal photoreceptors (α-opic irradiances) [4], [39].

The data clearly identifies the pchip smoothed profile as the best reconstruction method. For the AS7341 and AS7343 sensors using the pchip method, the error remains consistently below 11 % for illuminance and all photoreceptor-weighted irradiances. Even for the lower-resolution AS7262, the last method significantly reduces the error compared to the Envelope and Regularised approaches.

To contextualise these results, commercial spectroradiometers typically aim for uncertainties in the 5 % to 10 % range. For instance, the Apogee MS-100 (approx. 2000 €) specifies an irradiance accuracy of ±10 %, while the higher-end Apogee PS-200 (approx. 6000 €) offers ±5 % accuracy. The AS7341 and AS7343,

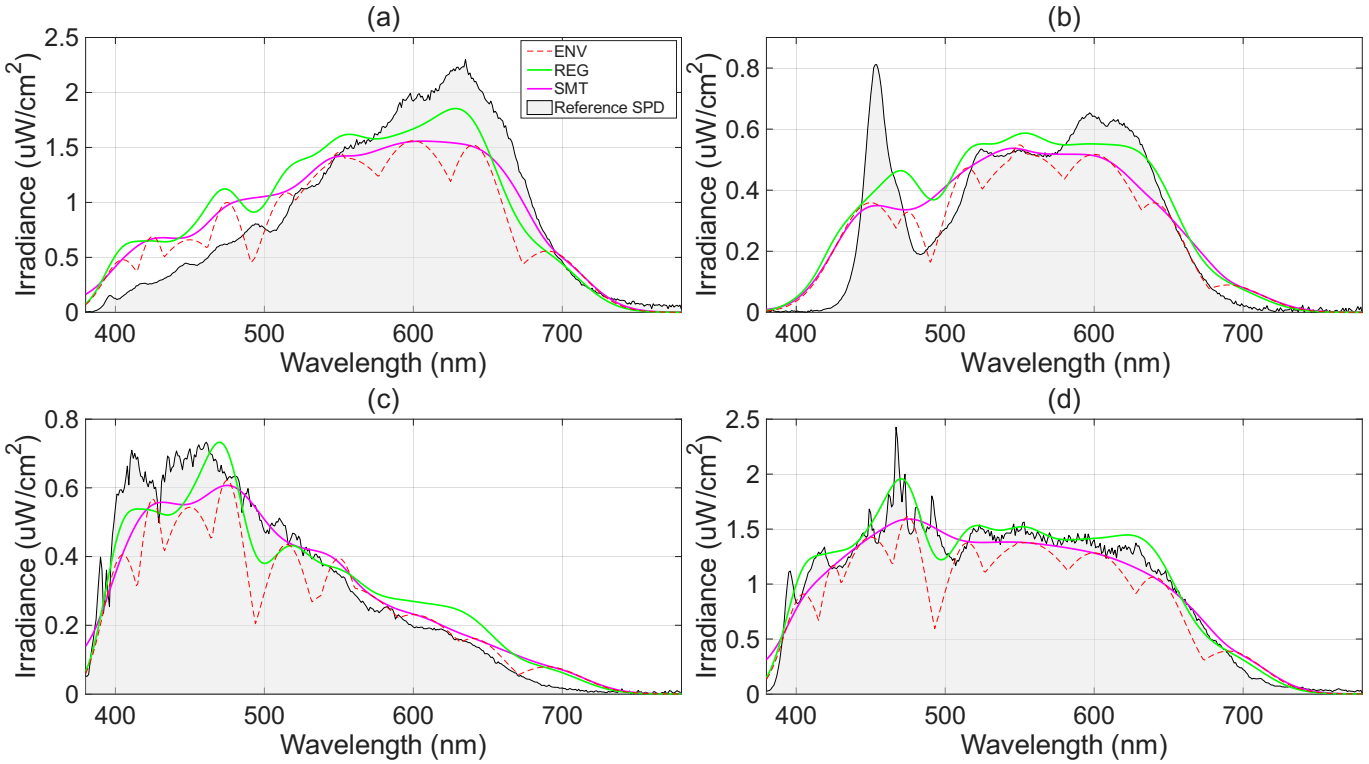

Figure 3. SPD reconstruction for AS7343 spectrometer under alogen (a), LED (b), sunlight (c) and xenon (d) illumination. Note that, for visualization purposes, the y axis has not the same range in the four plots

Table 6. Root Mean Square Error (RMSE) and relative error (%) of derived photometric and colorimetric quantities for the three reconstruction methods (Envelope, Regularised, Pchip) across the three sensors.

	AS7262			AS7341			AS7343		
Metric	ENV	REG	SMT	ENV	REG	SMT	ENV	REG	SMT
Mean RMSE	0.3827	0.2438	0.1846	0.2950	0.1444	0.1289	0.2343	0.1385	0.1284
Spectral Irradiance Error (%)	31.13	19.36	16.48	19.48	9.36	9.17	15.90	10.20	9.28
Illuminance Error (%)	22.23	14.10	8.79	17.19	7.73	6.45	13.47	8.68	7.71
S-cone Irradiance Error (%)	28.56	23.60	15.99	21.51	13.37	10.22	13.80	12.14	9.20
M-cone Irradiance Error (%)	22.81	14.44	7.72	17.71	8.35	7.11	14.05	8.78	7.67
L-cone Irradiance Error (%)	21.88	13.85	9.10	17.01	7.45	6.16	13.21	8.64	7.72
Rhodopic Irradiance Error (%)	28.35	18.44	9.41	19.45	10.86	9.23	17.26	11.07	8.43
Melanopic Irradiance Error (%)	30.62	20.00	11.02	20.19	12.02	10.06	18.79	11.91	8.91

when paired with the proposed calibration and right reconstruction, achieve performance comparable to the MS-100 at a fraction of the cost.

Finally, the dynamic range of the three sensors was determined based on theoretical considerations, as an accurate experimental measurement would necessitate an extensive sweep of source conditions. By considering the full sweep of available gain and integration time settings, defining the valid saturation level at 80 % of the ADC full scale, and excluding configurations with high noise, the analysis reveals distinct operating windows for each device. The AS7262 supports an irradiance range from approximately 95 $\mu W/cm^2$ to 1.5 W/cm^2. The AS7343 offers a significantly broader range, spanning from 200 nW/cm^2 to 12 W/cm^2, while the AS7341 covers an intermediate but similarly wide range from 800 nW/cm^2 to 10 W/cm^2. This difference is given by the internal configurations available, since the AS7343 is the one with the highest possible gain, 2048X, and the AS7262 only support a limited number of integration time compared to the other two sensors. Anyway, each sensor provide enough dynamic range to cover typical.

4.4. Experiment 3: Responsivity stability using Different Light Sources

As stated in Section 3.7., to validate the robustness of the radiometric calibration, the quadratic model was tested against a composite dataset comprising measurements from three spectrally distinct light sources: the Xenon arc lamp, a Halogen lamp, and a white LED (Dataset 2). This validation step assesses whether each spectral channel responds solely to the total optical power P_i absorbed within its sensitivity range, rather than to the specific spectral shape of the incident light $E(\lambda)$.

The quadratic coefficients (a_i, b_i) were recalculated using the least-squares method on the Dataset 2 and compared against the baseline coefficients obtained from the Dataset 1. Table 7 details this comparison, including the 95 % confidence bounds for the Dataset 1 fitting.

Table 7. Comparison of calibration coefficients a_i and b_i between the Dataset 1 baseline and the Dataset 2. The Dataset 2 coefficients generally align well with the Dataset 1 95% Confidence Bounds (CB).

Sensor	Ch	a_i coefficient (10^{-5})		b_i coefficient (10^{-3})	
		Dataset 1 [95% CB]	Dataset 2	Dataset 1 [95% CB]	Dataset 2
AS7262	1	9.44 [8.44 - 10.44]	12.51	42.15 [41.17 - 43.13]	39.36
	2	9.38 [8.40 - 10.35]	10.27	45.84 [44.92 - 46.77]	44.77
	3	8.91 [7.54 - 10.28]	5.91	52.93 [51.65 - 54.22]	56.52
	4	10.80 [9.89 - 11.71]	12.92	59.34 [58.49 - 60.19]	57.20
	5	22.27 [19.60 - 24.94]	13.09	47.88 [45.52 - 50.25]	54.33
	6	21.19 [16.83 - 25.54]	57.82	55.41 [52.59 - 58.22]	25.35
AS7341	1	2.09 [1.82 - 2.35]	2.17	6.44 [6.30 - 6.58]	6.38
	2	1.91 [1.66 - 2.16]	1.73	8.20 [8.01 - 8.39]	8.38
	3	1.83 [1.51 - 2.15]	1.90	9.72 [9.41 - 10.02]	9.63
	4	2.35 [2.12 - 2.57]	2.23	12.14 [11.93 - 12.35]	12.28
	5	2.62 [2.49 - 2.75]	2.69	13.66 [13.54 - 13.79]	13.58
	6	2.50 [2.20 - 2.79]	2.50	14.87 [14.58 - 15.16]	14.87
	7	2.79 [2.46 - 3.12]	2.86	15.58 [15.24 - 15.92]	15.50
	8	4.16 [3.80 - 4.52]	3.91	9.97 [9.77 - 10.16]	10.04
AS7343	1	15.25 [13.61 - 16.89]	14.07	7.53 [6.77 - 8.28]	8.22
	2	16.23 [14.65 - 17.80]	14.16	7.73 [7.04 - 8.42]	8.73
	3	1.60 [1.34 - 1.85]	1.36	5.59 [5.26 - 5.92]	5.99
	4	6.15 [5.19 - 7.10]	5.66	7.49 [6.70 - 8.27]	8.00
	5	4.02 [3.32 - 4.73]	2.71	8.24 [7.60 - 8.88]	9.76
	6	5.15 [4.64 - 5.67]	4.67	2.66 [2.23 - 3.08]	3.02
	7	0.89 [0.76 - 1.03]	0.81	4.85 [4.54 - 5.17]	5.10
	8	1.27 [1.04 - 1.49]	1.35	5.70 [5.32 - 6.08]	5.53
	9	5.34 [4.65 - 6.03]	6.63	8.68 [8.06 - 9.30]	7.19
	10	34.12 [30.82 - 37.42]	28.84	3.67 [2.45 - 4.89]	5.60

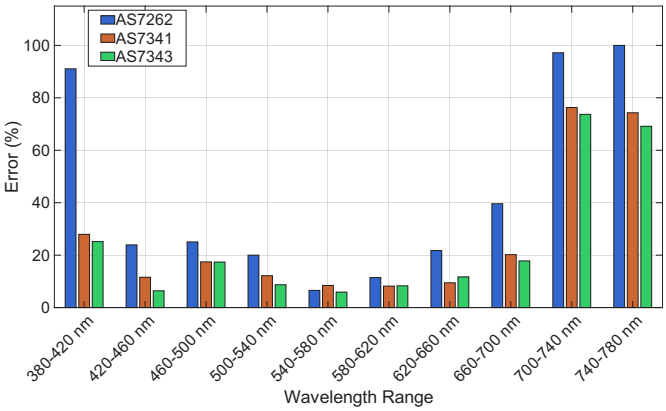

Figure 4. Spectral distribution of the relative reconstruction error (%) for the AS7262 (blue), AS7341 (red) and AS7343 (green) sensors. The error is averaged between each reconstruction method and then across 40 nm spectral bins to highlight performance variations across the visible range.The high error bars correspond to wavelength values that lie outside the sensitivity range of the three sensors.

The results demonstrate great stability. Despite the significant variation in spectral power distribution among the sources, the coefficients obtained from the Dataset 2 fall consistently within or very close to the 95 % confidence bounds of the Dataset 1 calibration (as seen clearly in the AS7341 and AS7343 data). This confirms that the spectral reconstruction method is source-independent and that the coefficients (a_i, b_i) derived in Eq. 6 are intrinsic to the sensor's response rather than artifacts of a specific calibration source.

To further evaluate the system's robustness, the reconstruction capabilities were assessed using the calibration derived from Dataset 2. The figures of merit established in Experiment 2 were calculated specifically for the smooth (SMT) reconstruction profile, which was identified as the optimal fitting method in Section 4.3.. The resulting metrics are detailed in Table 8. The fitting performance remains highly comparable to the primary dataset, with error metrics and RMSE values varying by only approximately 1 % to 2 % relative to the Dataset 1 results. This consistency highlights that the sources employed in Dataset 2, despite their spectral differences, were sufficiently broadband and covered a wide enough dynamic range of irradiance to allow the quadratic fitting to be performed with high fidelity.

Table 8. Root Mean Square Error (RMSE) and relative error (%) derived from the Smooth (SMT) reconstruction profile, using the quadratic parameters extracted from Dataset 2 fitting.

Metric	AS7262	AS7341	AS7343
Mean RMSE	0.1770	0.1282	0.1249
Spectral Irradiance Error (%)	11.98	8.98	8.82
Illuminance Error (%)	6.12	6.34	7.64
S-cone Irradiance Error (%)	15.09	10.22	9.98
M-cone Irradiance Error (%)	6.40	7.02	8.16
L-cone Irradiance Error (%)	5.99	6.05	7.41
Rhodopic Irradiance Error (%)	9.45	9.26	9.09
Melanopic Irradiance Error (%)	11.10	10.09	9.59

5. CONCLUSION

This work presented a systematic and application-oriented evaluation of compact multi-spectral sensors, with the specific goal of defining a calibration methodology that is robust, reproducible, and easily transferable across laboratories and field deployments. The proposed approach was intentionally designed to rely on a minimal experimental setup and broadly available instrumentation, in order to promote consistent use of these devices as quantitative illuminance meters for daily-life light monitoring in both indoor and outdoor environments.

Three commercially available sensors with different spectral architectures—the AS7262, AS7341, and AS7343—were systematically evaluated using a common optical setup and reference

instrumentation (Section 3.). This enabled a direct comparison of their radiometric behaviour, spectral reconstruction capability, and practical operating limits, while keeping the calibration workflow general enough to be reproduced on other multi-channel devices.

A first key outcome concerns dynamic range management. As shown in Experiment 1 (Section 4.1.), adjusting sensitivity via integration time at constant gain yields a highly stable response, with the coefficient of variation $\tilde{CV}(t_{\mathrm{int}})$ consistently on the order of 10^{-4} across all sensors. Conversely, when sensitivity is adjusted by varying the analogue gain at constant integration time, the coefficient of variation $\tilde{CV}(G)$ increases by up to two orders of magnitude, reaching values on the order of 10^{-2}. This behaviour indicates increased variability and gain-dependent non-linearities, which hinder the definition of a robust, global radiometric calibration. Accordingly, to preserve measurement stability while maximising dynamic range, the analogue gain should be fixed and exposure regulated exclusively through the integration time.

Building on this configuration choice, Experiment 2 (Section 3.5.) established an absolute radiometric calibration using a broadband Xenon arc lamp as the excitation source. A quadratic model was adopted to link normalised counts to the effective optical power absorbed by each channel. The fitted models showed excellent agreement with the experimental data ($R^2 > 0.998$ for all channels), enabling accurate estimation of channel responsivity using broadband illumination only.

The subsequent validation under real-world illumination conditions (Section 3.6.) demonstrated that, once calibrated, the sensors can reliably reconstruct the spectral power distribution of broadband light sources and derive accurate estimates of spectral irradiance, illuminance, and α-opic irradiances. Among the tested reconstruction strategies, the smoothed PCHIP (SMT) interpolation consistently provided the best compromise between accuracy and generality. For the AS7341 and AS7343, this approach yielded illuminance and photoreceptor-weighted irradiance errors typically below 11 %, with average errors across all reported metrics of approximately 8.3 % and 8.0 %, respectively (Table 6). These results also clarify the role of channel density and distribution. Increasing the number of channels improves reconstruction accuracy primarily when the channels are well distributed and approximately equispaced over the spectral range. The transition from the six visible channels of the AS7262 to the denser visible sampling of the AS7341 and AS7343 leads to a substantial reduction in reconstruction error, with average SMT errors decreasing from approximately 11 % for the AS7262 to below 9 % for the other two sensors. In contrast, the three additional channels of the AS7343, which largely overlap with those of the AS7341, provide only marginal improvements, confirming that channel redundancy yields diminishing returns for broadband spectral reconstruction.

Experiment 3 (Section 3.7.) further showed that the proposed calibration is largely independent of the spectral shape of the calibration source, provided that the illumination spans the sensor sensitivity range and a sufficient dynamic range of irradiance. The stability of the quadratic coefficients across spectrally distinct sources confirms that the sensor response depends primarily on the integrated optical power absorbed within each channel, rather than on the detailed spectral distribution of the incident light.

At the same time, intrinsic limitations remain. Due to their interference-filter-based design, these sensors cannot accurately resolve narrow spectral features, as sharp emission peaks are unavoidably broadened by the channel response. As a result, they are not intended to replace high-resolution spectrometers in applications requiring fine spectral discrimination. Their effectiveness is maximised in broadband lighting conditions typical of indoor and outdoor environments, or in scenarios where prior knowledge of the source class is available.

In summary, this paper provides a complete and reproducible workflow for configuring, calibrating, and validating compact multi-spectral sensors as quantitative illuminance meters. By combining a minimal calibration setup, a robust radiometric model, and application-oriented reconstruction strategies, the proposed methodology clarifies both the achievable accuracy and the practical limits of these devices, supporting their use in wearable, portable, and distributed light-sensing applications.

AUTHORS' CONTRIBUTION

A. B.: Investigation, Software, Formal analysis, Writing – original draft.
G. G.: Methodology, Formal analysis, Writing – original draft, Writing – review & editing.
L. R.: Resources, Funding acquisition, Supervision.
A. G.: Conceptualization, Methodology, Funding acquisition, Writing – original draft, Writing – review & editing.

SOFTWARE AND DATA AVAILABILITY

All software tools and the complete dataset produced in the course of this study will be openly available at: https://github.com/OPTOLAB-UNIMORE/Calibration-Method-for-Multi-Channel-Sensor

REFERENCES

[1] J. van Duijnhoven, S. Hartmeyer, A. Didikoglu, O. Stefani, K. W. Houser, V. Kalavally, M. Spitschan, Measuring light exposure in daily life: A review of wearable light loggers, Building and Environment, 2025, p. 112771.
DOI: 10.1016/j.buildenv.2025.112771

[2] G. K. Agbeshie, I. O. D. Junior, A. K. A. Andoh, J. Ampong, N. A. O. Mensah, A. Y. Ampoma-Mensah, J. Zauner, M. Spitschan, K. O. Akuffo, Physiologically relevant real-world light exposure and its behavioural and environmental determinants in Kumasi, Ghana, Open Research Europe, vol. 5, 2025, p. 300.
DOI: 10.12688/openreseurope.21304.1

[3] A. M. Biller, J. Zauner, C. Cajochen, M. A. Gerle, V. Kalavally, A. Mohamed, L. Rottländer, M.-Y. Seah, O. Stefani, M. Spitschan, Physiologically-relevant light exposure and light behaviour in Switzerland and Malaysia, bioRxiv, 2025, pp. 2025–01.
DOI: 10.1101/2025.01.07.631760

[4] R. J. Lucas, S. N. Peirson, D. M. Berson, T. M. Brown, H. M. Cooper, C. A. Czeisler, M. G. Figueiro, P. D. Gamlin, S. W. Lockley, J. B. O'Hagan, L. L. A. Price, I. Provencio, D. J. Skene, G. C. Brainard, Measuring and using light in the melanopsin age, Trends in Neurosciences, vol. 37, Jan. 2014, no. 1, pp. 1–9.
DOI: 10.1016/j.tins.2013.10.004

[5] J. S. Botero-Valencia, J. Valencia-Aguirre, D. Durmus, A low-cost IoT multi-spectral acquisition device, HardwareX, vol. 9, Apr. 2021, p. e00173.
DOI: 10.1016/j.ohx.2021.e00173

[6] J. S. Botero-Valencia, J. Valencia-Aguirre, D. Durmus, W. Davis, Multi-channel low-cost light spectrum measurement using a multilayer perceptron, Energy and Buildings, vol. 199, Sep. 2019, pp. 579–587.
DOI: 10.1016/j.enbuild.2019.07.026

[7] P. Myland, S. Babilon, T. Hegemann, S. Klir, T. Q. Khanh, Reconstruction of spectral irradiance in a real application with a multichannel spectral sensor using convolutional neural networks, Optics Express, vol. 31, Jul. 2023, no. 16, pp. 25 724–25 746.
DOI: 10.1364/OE.489449

[8] T. Kristiansen, T. K. Thiis, I. Burud, A. J. Petersen, Enabling scalable, human-centric daylight assessment: A validated open-source platform for spatial-spectral monitoring in buildings, Available at SSRN 5653714, 2025.
DOI: 10.2139/ssrn.5653714

[9] D. D. W. Ren, S. Tripathi, L. K. B. Li, Low-cost multispectral imaging for remote sensing of lettuce health, Journal of Applied Remote Sensing, vol. 11, Jan. 2017, no. 1, p. 016006.
DOI: 10.1117/1.JRS.11.016006

[10] V. Lebourgeois, A. Bégué, S. Labbé, M. Houlès, J. F. Martiné, A light-weight multi-spectral aerial imaging system for nitrogen crop monitoring, Precision Agriculture, vol. 13, Oct. 2012, no. 5, pp. 525–541.
DOI: 10.1007/s11119-012-9262-9

[11] P. Lopin, P. Nawsang, S. Laywisadkul, K. V. Lopin, Evaluation of Low-Cost Multi-Spectral Sensors for Measuring Chlorophyll Levels Across Diverse Leaf Types, Sensors, vol. 25, Jan. 2025, no. 7, p. 2198.
DOI: 10.3390/s25072198

[12] J. D. Stevens, D. Murray, D. Diepeveen, D. Toohey, Adaptalight: An inexpensive par sensor system for daylight harvesting in a micro indoor smart hydroponic system, Horticulturae, vol. 8, 2022, no. 2, p. 105.
DOI: 10.3390/horticulturae8020105

[13] J. Larochelle, J. Klueppel, R. McCormick, K. Biegert, L. M. Comella, A low-power optical sensor with dynamically adjustable field of view for photosynthetically active radiation (par) measurement, IEEE Sensors Journal, vol. 24, 2024, no. 6, pp. 7711–7728.
DOI: 10.1109/jsen.2024.3361086

[14] O. Hadj Abdelkader, H. Bouzebiba, D. Pena, A. P. Aguiar, Energy-Efficient IoT-Based Light Control System in Smart Indoor Agriculture, Sensors, vol. 23, Jan. 2023, no. 18, p. 7670.
DOI: 10.3390/s23187670

[15] G. Liu, Z. Ma, Study on a novel portable urine analyzer based on optical fiber bundles, Measurement, vol. 130, 2018, pp. 412–421.
DOI: 10.1016/j.measurement.2018.08.037

[16] J. T. Givans, A. Waswa, J. Madete, J. M. Pearce, Open-source light calibration system for hyperbilirubinemia phototherapy treatments, medRxiv, 2025, pp. 2025–08.
DOI: 10.1101/2025.08.01.25332669

[17] T.-N. Nguyen, Q.-H. Pham, D.-K. Nguyen, H.-M. Nguyen, T.-L. Le Ho, Q.-A. Le, N.-T. Tran, Painless and accurate ai-driven method for personal glucose tracking based on multi-spectral sensing, International Conference on Intelligent Systems and Data Science, Springer, 2025, pp. 133–146.
DOI: 10.1007/978-981-95-3355-8_10

[18] Z. Ye, Z. Huang, J. Zhou, H. Li, M. Zhang, Q. He, H. Chen, J. Zhong, H. Zhang, Z. Han, L. T. Chu, W. Guo, A portable optical device for quantitative detection of lithium in blood plasma, Anal. Methods, vol. 17, 2025, pp. 5355–5361.
DOI: 10.1039/D5AY00469A

[19] F. J. Bolton, A. S. Bernat, K. Bar-Am, D. Levitz, S. Jacques, Portable, low-cost multispectral imaging system: Design, development, validation, and utilization, Journal of Biomedical Optics, vol. 23, Dec. 2018, no. 12, p. 121612.
DOI: 10.1117/1.JBO.23.12.121612

[20] A. Amirazar, M. Azarbayjani, M. Molavi, M. Karami, A low-cost and portable device for measuring spectrum of light source as a stimulus for the human's circadian system, Energy and Buildings, vol. 252, 2021, p. 111386.
DOI: 10.1016/j.enbuild.2021.111386

[21] A. Mohamed, V. Kalavally, S. W. Cain, A. J. Phillips, E. M. McGlashan, C. P. Tan, Wearable light spectral sensor optimized for measuring daily α-opic light exposure, Optics Express, vol. 29, 2021, no. 17, pp. 27 612–27 627.
DOI: 10.1364/oe.431373

[22] J. Stampfli, B. Schrader, C. Di Battista, R. Häfliger, O. Schälli, G. Wichmann, C. Zumbühl, P. Blattner, C. Cajochen, R. Lazar et al., The light-dosimeter: A new device to help advance research on the non-visual responses to light, Lighting Research & Technology, vol. 55, 2023, no. 4-5, pp. 474–486.
DOI: 10.1177/14771535221147140

[23] G. Gibertoni, A. Hromov, F. Piffaretti, M. H. Geiser, Development of an Innovative Pupillometer Able to Selectively Stimulate the Eye's Fundus Photoreceptor Cells, Diagnostics, vol. 14, Jan. 2024, no. 17, p. 1940.
DOI: 10.3390/diagnostics14171940

[24] M. Spitschan, A. M. Biller, K. Broszio, E. Fischer, J. Hegewald, S. Rabstein, E. Saathoff, K. Smolders, S. M. Thalji, S. Weigelt, D. Weiskopf, J. Zauner, Ocular light and optical radiation exposure as a modifiable environmental determinant of health: Expert consensus on research gaps and priorities, medRxiv, Nov. 2025, p. 2025.08.27.25333976.
https://www.medrxiv.org/content/early/2025/11/17/2025.08.27.25333976.
DOI: 10.1101/2025.08.27.25333976

[25] N. Mohammadian, A. Didikoglu, C. Beach, P. Wright, J. W. Mouland, F. P. Martial, S. Johnson, M. Van Tongeren, T. M. Brown, R. J. Lucas et al., A wrist-worn internet of things sensor node for wearable equivalent daylight illuminance monitoring, IEEE Internet of Things Journal, vol. 11, 2024, no. 9, pp. 16 148–16 157.
DOI: 10.1109/jiot.2024.3355330

[26] A. Gibaldi, V. DuTell, M. S. Banks, Solving parallax error for 3d eye tracking, ACM Symposium on eye tracking research and applications, 2021, pp. 1–4.
DOI: 10.1145/3450341.3458494

[27] W. W. Sprague, E. A. Cooper, S. Reissier, B. Yellapragada, M. S. Banks, The natural statistics of blur, Journal of Vision, vol. 16, 2016, no. 10, pp. 23–23.
DOI: 10.1167/16.10.23

[28] V. DuTell, A. Gibaldi, G. Focarelli, B. A. Olshausen, M. S. Banks, High-fidelity eye, head, body, and world tracking with a wearable device, Behavior Research Methods, vol. 56, 2024, no. 1, pp. 32–42.
DOI: 10.3758/s13428-022-01888-3

[29] A. Gibaldi, E. N. Harb, C. F. Wildsoet, M. S. Banks, A child-friendly wearable device for quantifying environmental risk factors for myopia, Translational Vision Science & Technology, vol. 13, 2024, no. 10, pp. 28–28.
DOI: 10.1167/tvst.13.10.28

[30] ams OSRAM, As7262 6-channel visible spectral id sensor, 2017, datasheet: AS7262 Spectral ID Sensor, Document DS000486 Rev. 5-00.
https://ams-osram.com/products/sensor-solutions/ambient-light-color-spectral-proximity-sensors/ams-as7262-consumer-grade-smart-6-channel-vis-sensor

[31] ams OSRAM, ams AS7341 11-Channel Spectral Color Sensor, 2022.
https://ams-osram.com/products/sensor-solutions/ambient-light-color-spectral-proximity-sensors/ams-as7341-11-channel-spectral-color-sensor

[32] ams OSRAM, ams AS7343 14-Channel Spectral Sensor, 2021.
https://ams-osram.com/products/sensor-solutions/ambient-light-color-spectral-proximity-sensors/ams-as7343-spectral-sensor

[33] Ocean Optics, Hl-2000 tungsten halogen light source, 2013, installation and Operation Manual, Document 000-10000-050-02-201307 (Copyright © 2009).
https://www.oceaninsight.com

[34] Cree LED, Xlamp mx-6 led: Product data sheet (cld-ds23, rev. 12a), 2025, © 2009–2025 Cree LED. Document CLD-DS23, Revision 12A.
https://www.cree-led.com

[35] Thorlabs, Fesh0900: Ø25 mm shortpass filter, 900 nm cut-off, 2020.

[36] Thorlabs, Ndc-50s-1 unmounted step variable nd filter, Ø50 mm, od: 0.04-1.0, 2004, coating: Inconel metallic ND; 2 mm thickness; diameter tolerance +0/-0.25 mm; not intended as laser safety equipment.
https://www.thorlabs.com/thorproduct.cfm?partnumber=NDC-50S-1

[37] Broadcom Limited, AFBR-S20M2WU, 2023, qmini Wide UV configuration, spectral resolution 1.5 nm, 50 mm focal length, SMA input slit, exposure time 3-600 s.

https://www.broadcom.com/products/optical-sensors/spectrometers/spectrometers-qmini/afbr-s20m2wu

[38] Thorlabs, Thorlabs PM16-130 USB Power Meter, Slim Photodiode Sensor, Si 400-1100 nm, 2015.
https://www.thorlabs.com/thorproduct.cfm?partnumber=PM16-130

[39] Commission Internationale de l'Eclairage (CIE), CIE S 026/E:2018 CIE System for Metrology of Optical Radiation for ipRGC-Influenced Responses to Light, Color Research & Application, vol. 44, 2019, no. 2.
DOI: 10.1002/col.22350